Rock and Soil Mechanics

Volume 42 | Issue 9 Article 9

12-14-2021

Numerical analysis of seismic damage characteristics of an underground cavern intersected by a steeply dipped fault

Shi-jie CHEN
Key Laboratory of Rock Mechanics in Hydraulic Structural Engineering, Ministry of Education, Wuhan University, Wuhan, Hubei 430072, China

Ming XIAO
Key Laboratory of Rock Mechanics in Hydraulic Structural Engineering, Ministry of Education, Wuhan University, Wuhan, Hubei 430072, China, mxiao@whu.edu.cn

Xiao-wei WANG
Changjiang Institute of Survey, Planning, Design and Research, Wuhan, Hubei 430010, China

Jun-tao CHEN
Key Laboratory of Rock Mechanics in Hydraulic Structural Engineering, Ministry of Education, Wuhan University, Wuhan, Hubei 430072, China

Follow this and additional works at: https://rocksoilmech.researchcommons.org/journal

 Part of the Geotechnical Engineering Commons

Custom Citation

CHEN Shi-jie, XIAO Ming, WANG Xiao-wei, CHEN Jun-tao, . Numerical analysis of seismic damage characteristics of an underground cavern intersected by a steeply dipped fault[J]. Rock and Soil Mechanics, 2021, 42(9): 2600-2610.

This Article is brought to you for free and open access by Rock and Soil Mechanics. It has been accepted for inclusion in Rock and Soil Mechanics by an authorized editor of Rock and Soil Mechanics.

Rock and Soil Mechanics 2021 42(9): 2600−2610 ISSN 1000−7598
https: //doi.org/10.16285/j.rsm.2020.6886 rocksoilmech.researchcommons.org/journal

Numerical analysis of seismic damage characteristics of an underground cavern intersected by a steeply dipped fault

CHEN Shi-jie[1, 2], XIAO Ming[1, 2], WANG Xiao-wei[3], CHEN Jun-tao[1, 2]

1. State Key Laboratory of Water Resources and Hydropower Engineering Science, Wuhan University, Wuhan, Hubei 430072, China
2. Key Laboratory of Rock Mechanics in Hydraulic Structural Engineering, Ministry of Education, Wuhan University, Wuhan, Hubei 430072, China
3. Changjiang Institute of Survey, Planning, Design and Research, Wuhan, Hubei 430010, China

Abstract: The steeply dipped fault zone is the weak link of the seismic stability of underground caverns. Aimed at the complex dynamic interaction characteristics between the surrounding rock and fault, based on the Ladanyi's shear strength model, the seismic deterioration coefficient was introduced, and a shear strength model considering nonlinear mechanical properties and seismic deterioration effect was established. Further considering the discontinuous deformation characteristics between surrounding rock and faults, a three-dimensional dynamic contact force method was proposed considering both the complex shear strength and multiple contact states. The method was applied to the Jinchuan underground powerhouse to study its seismic damage characteristics under the influence of the steeply dipped fault F31. The results indicate that after considering the interface and seismic deterioration effects, the seismic response of the cavern increases, the dislocation between the surrounding rock and fault is more evident, and a certain depth of separation and sliding failure zones occurs. The steeply dipped fault cuts the high sidewalls of the main workshop, and forms a weak zone where the surrounding rock thickness is thin. The weak zone has more significant deformation and damage, and is prone to flexural toppling deformation and slipping deformation into the cavern on the upstream and downstream sidewalls, respectively. The distribution of the sliding and separation failure zone of the interfaces between the surrounding rock and fault are dynamic changes during the seismic process, and it continues to extend to the deep. Among them, the separation zone is relatively large at the arch abutment and rock anchoring beam. The numerical results reveal the dynamic failure mechanism of the surrounding rock of the underground cavern intersected by a steeply dipped fault, which can provide a reference for the seismic design.

Keywords: underground cavern; steeply dipped fault; dynamic contact method; seismic response; damage characteristics

1 Introduction

Numerous underground powerhouses and tunnel projects for national strategic needs are being developed in the southwest of China. Due to the complex geological structure and strong crustal movement in the southwest valley areas, underground caverns will inevitably encounter weak fault zones and high seismic intensity zones during construction. Engineering practice has proven that unfavorable geological structures such as faults play a major role in controlling strong seismic damage of underground caverns[1−2]. The relative movement of surrounding rocks and faults can be triggered easily by earthquakes, causing unrecoverable damage to caverns and affecting their regular operation. Compared with tunnels, underground powerhouses are characterized by high sidewalls and long spans, and their fault fracture zones are the weak links of seismic resistance. Therefore, it is of great significance to study the seismic failure characteristics of underground caverns intersected by faults for the seismic design and safe operation.

Many scholars have studied the seismic responses of underground caverns under fault action by means of field investigation[3], physical experiment[4] and numerical simulation. Among them, the numerical simulation method has been widely used due to its low computational cost, high efficiency and ability to simulate complex nonlinear boundaries[5−6]. He et al.[7] and Li et al.[8] studied the seismic response characteristic and damage mechanism of a tunnel through fault zone, based on finite difference method and structural plane element. Zhao et al.[9] studied the seismic response of a cross-fault tunnel under P-wave through numerical simulation. Using the discrete element method, Yang et al.[10] investigated the seismic damage process of a tunnel−fault system. Ardeshirilajimi et al.[11] implemented a hybrid finite difference-discrete element method to perform nonlinear dynamic analysis of underground caverns under the influence of a single fault layout. Cui et al.[12] used the discrete element method to investigate the effect of discontinuous interlayer dislocation zone on the stability of the surrounding rocks of the powerhouse at Baihetan under seismic loading. It can

Received: 18 October 2020-12-18 Received: 8 May 2021
This work was supported by the National Natural Science Foundation of China(52079097, 51579191) and the National Key R & D Program of China (2015CB057904).
First author: CHEN Shi-jie, male, born in 1993, PhD candidate, mainly engaged in numerical simulation of underground engineering stability under complex conditions. E-mail: chenjexich@whu.edu.cn
Corresponding author: XIAO Ming, male, born in 1957, PhD, Professor, doctoral supervisor, mainly engaged in the research of underground engineering stability. E-mail: mxiao@whu.edu.cn

be found from the existing studies that fault increases the failure depth of surrounding rock and causes discontinuity of displacement and stress around the cavern, thus increasing its instability. There are many achievements in tunnel engineering, but few researches on the dynamic damage characteristics of underground caverns with high sidewalls and large spans under the influence of faults. Meanwhile, although most studies simulate the dislocation of surrounding rock and fault under seismic loading, they ignore the deterioration effect of cyclic seismic load on the strength of the interface between surrounding rock and fault.

Dadu River Jinchuan hydropower station located in Sichuan province is a vital hydropower project in Southwest China. A steeply dipped fault F31 cuts the main workshop, and the angle of intersection between the strike of the fault and the axis of the workshop is 36º. The dip angle of the fault and its intersection angle with the carven axis greatly influence the seismic response of carven[13−14]. For steeply inclined structural planes, Zhang et al.[15] and Li et al.[16] studied the influences on the surrounding rock stability relying on Dagang Mountain and Wudongde underground workshops, respectively, and showed that surrounding rock failure controlled by structural planes is prone to occur in the static excavation. It can be predicted that the 'small included angle and steep dip' F31 fault has a more significant influence on the dynamic stability of the main workshop with a high sidewall and large span, which is the weak area of surrounding rock and plays a controlling role in the seismic stability of Jinchuan main workshop. At present, there have been few research findings regarding this field. Therefore, it is of great significance to study the seismic damage characteristics of the Jinchuan underground powerhouse under the action of steep dip faults.

In this study, a complex shear strength model of the interface between surrounding rock and fault under seismicity is established, considering nonlinear mechanical properties and seismic deterioration effect. Then, a three-dimensional dynamic contact force algorithm considering complex shear strength and multiple contact states is proposed for the complex dynamic contact behavior of surrounding rock and fault. Taking Jinchuan underground powerhouse as an example, the influence of steeply dipped fault on the seismic response of the main powerhouse is analyzed. The dynamic failure mechanism of surrounding rock is discussed, which is expected to provide a helpful reference for seismic engineering design.

2 Shear strength model of interface between surrounding rock and fault

The shear strength of the contact surface between surrounding rock and fault is a crucial parameter controlling the deformation and failure of surrounding rock. Its contact surface is irregular and rough in the natural state, and in the closed state, irreversible shear damage such as abrasion or shearing commonly occurs, exhibiting a nonlinear shear strength[17]. The phenomenon of dynamic strength attenuation of rock structure planes due to dynamic seismic action has also been confirmed by numerous experiments[18]. However, the Mohr−Coulomb shear strength model commonly used in dynamic analysis cannot reflect these phenomena. Therefore, it is necessary to establish a shear strength model for the contact surface between surrounding rock and fault considering nonlinear mechanical properties and seismic deterioration effect.

2.1 Nonlinear shear strength formula

Under static conditions, the shear strength of the contact surface between the surrounding rock and fault is mainly affected by its geometry and stress state. When the normal stress or undulating angle of the contact surface is minor, the climbing effect and abrasion are likely to occur. In contrast, shearing tends to occur when the normal stress or undulating angle is large. Through a large number of natural joint shear tests, Barton et al.[19] used joint roughness to describe the geometry of structural surfaces and proposed a JRC-JCS shear strength model. Patton[20] simplified the discontinuity surface into a regular sawtooth shape and proposed a bilinear strength theory with concise formula. Ladanyi et al.[21] pointed out that the structural plane is irregular and the strength envelope is a curve, and proposed the corresponding strength model according to the theory and experiment. Grasselli et al.[22], Ghazvinian et al.[23] also proposed strength models considering the geometry of structural planes, but due to the complicated parameters, it has not been widely used in engineering.

Due to the low strength of rock mass near weak faults, its shear failure is more likely to occur during the interaction with surrounding rocks, which plays a leading role in the shear strength of the contact surface[24]. The strength model proposed by Ladanyi et al.[21] comprehensively considered the geometric parameters of the interface and the influence of rock strength. Compared with Patton's model, it has a better imitative effect on the structural planes prone to shear failure[17]. Hence, based on Ladanyi strength Model[21], a strength model for the contact surface between surrounding rock and fault is established in this study. Its peak shear strength τ_{p} can be expressed as

$$\tau_{\mathrm{p}}=\frac{\sigma(1-\alpha_{\mathrm{s}})(\dot{\nu}+\tan\varphi_{\mathrm{b}})+\alpha_{\mathrm{s}}\tau_{\mathrm{b}}}{1-(1-\alpha_{\mathrm{s}})\dot{\nu}\tan\varphi_{\mathrm{b}}} \tag{1}$$

$$\dot{\nu}=(1-\sigma/\sigma_{\mathrm{c}})^{K}\tan\theta \tag{2}$$

$$\alpha_{\mathrm{s}}=1-(1-\sigma/\sigma_{\mathrm{c}})^{L} \tag{3}$$

$$\tau_{\mathrm{b}} = \sigma \tan \varphi_{\mathrm{r}} + c_{\mathrm{r}} \quad (4)$$

where σ is the normal stress of contact surface; $\dot{v}$ is the dilatancy rate; α_{s} is the shearing rate representing the area ratio of shearing; σ_{c} is the uniaxial compressive strength of the bulge on contact surface; φ_{b} is the friction angle of contact surface; θ is the undulating angle; τ_{b}, φ_{r} and c_{r} are the shear strength, internal friction angle and cohesion of the convex part, respectively. For rough interfaces, the values of parameter K and L are 4.0 and 1.5, respectively[21]. If the strength of the fault zone is significantly weaker than that of the surrounding rock, the bulge can be considered as the fault zone rock from the safety point of view.

Because the contact surface between surrounding rock and fault is rough and irregular under natural states, and the undulating angle is not constant, they cannot be measured directly. Here, the dilatancy model proposed by Barton et al.[19] is adopted to calculate the undulating angle θ:

$$\theta = \theta_{\mathrm{p}} = \mathrm{JRC} \cdot \lg\left(\frac{\mathrm{JCS}}{\sigma}\right) \quad (5)$$

where θ_{p} is the peak dilatancy angle; JCS is the compressive strength of contact surface, and the compressive strength of the medium with weak strength is taken. JRC is the roughness coefficient of the contact surface, which is calculated by the method proposed by Yang et al.[25].

When the shear force of the contact surface exceeds its peak strength, the bond property of the contact surface is irreversibly damaged, and the contact surface presents a strain-softening phenomenon. The shear strength at this point is called residual shear strength, which is mainly provided by the friction of the bulge and can be expressed as

$$\tau_{\mathrm{r}} = \sigma \tan \varphi_{\mathrm{r}} \quad (6)$$

2.2 Seismic deterioration of contact surface strength

Seismic deterioration and attenuation of rock structural planes is a complex dynamic process. Seismic deterioration coefficient $D(t)$ is used to quantify the degradation degree of shear strength. Therefore, the peak shear strength $\tau_{\mathrm{p}}(t)$ and residual shear strength $\tau_{\mathrm{r}}(t)$ of the contact surface at time t can be defined as

$$\tau_{\mathrm{p}}(t) = D(t) \cdot t_{\mathrm{p0}}, \quad \tau_{\mathrm{r}}(t) = D(t) \cdot t_{\mathrm{r0}} \quad (7)$$

where τ_{p0} and τ_{r0} are the initial shear strength and initial residual shear strength of contact surface, respectively.

Previous studies have shown that the strength of the structural plane is mainly affected by two factors: cyclic seismic shear load and shear deformation rate[26−28]. In this paper, the influence coefficients of cyclic load $\eta(t)$ and shear deformation rate $\gamma(t)$ are adopted to quantitatively describe its influence ($\eta(t) \leqslant 1$、 $\gamma(t) \leqslant 1$). The former causes abrasion to the structural plane through cyclic shear frequency and amplitude, while the latter reduces the dynamic friction factor of the structural plane by generating relative velocity[28]. Assuming that during the earthquake, these two factors are mutually independent, the seismic deterioration coefficient of structural plane intensity $D(t)$ can be written as

$$D(t) = \eta(t) \cdot \gamma(t) \quad (8)$$

The cyclic shear frequency and amplitude of seismic load on the contact surface cause abrasion and passivation of the contact surface. The shear strength of the contact surface decreases gradually with time. Its influence on the strength of the contact surface obeys a negative exponential decay law with the seismic time[28−29]. Therefore, the influence coefficient of cyclic seismic load can be formulized as

$$\eta(t) = R_0 + (1 - R_0)\,\mathrm{e}^{-\xi(t/t_{\mathrm{s}})} \quad (9)$$

where R_0 is the convergence value of shear strength deterioration, $0 \leqslant R_0 < 1$; t_{s} is cumulative seismic time; ξ is the dimensionless undetermined coefficient. R_0 and ξ can be obtained from experiments.

The attenuation of shear deformation rate on the contact surface to shear strength also follow approximately negative exponential law, which can be expressed as[27]

$$\gamma(t) = m\left(|V(t)| + q\right)^{-p} \quad (10)$$

where $V(t)$ is the relative shear velocity of contact point pairs at time t; m, q and p are the dimensionless undetermined coefficients that can be estimated from experiments.

Therefore, the seismic deterioration coefficient $D(t)$ is gained as

$$D(t) = \left[R_0 + (1 - R_0)\,\mathrm{e}^{-\xi(t/t_{\mathrm{s}})}\right]\left[m\left(|V(t)| + q\right)^{-p}\right] \quad (11)$$

By integrating Eqs. (1), (6), (7) and (11), the complex nonlinear shear strength of the interface between surrounding rock and fault is received, which changes dynamically with the seismic process.

Compared with conventional models, the proposed shear strength model of the contact surface is more consistent with the reality of the shear strength of surrounding rock and fault interface under seismicity action. The undetermined parameters in the model can be determined by dynamic shear tests.

3 Analysis of discontinuous dynamics of surrounding rock and fault

During the earthquake, the interface between surrounding rock and fault is not only in a bonding contact

state but also may produce discontinuous states such as slip and detachment. Based on the explicit integral algorithm, this paper considers various contact states of surrounding rock and fault[30], and integrates the complex shear strength model in the previous section to establish a 3D dynamic contact force algorithm for contact surface, thus forming a discontinuous dynamic analysis method for surrounding rock and fault. The derivation is given below.

3.1 Explicit finite element integral method for contact system

Figure 1 shows two types of contact between surrounding rock and fault in three-dimensional space: point-to-point contact and point-to-surface contact. For undisturbed surrounding rocks, the contact surface is considered to be well cemented, and the node i on the fault and the node i' on the surrounding rock form the initial node pairs, known as point-to-point contact. After the disturbance, if the deformation of surrounding rock and fault is inconsistent, it is easy to slip along the contact surface. Under the circumstances, the node i on the fault corresponds to the node i' on a certain element surface of surrounding rock, and its contact form is point-to-surface contact. The contact forces of the two contact forms satisfy the interaction relation, i.e., $\boldsymbol{N}_i + \boldsymbol{N}_{i'} = \boldsymbol{0}$, $\boldsymbol{T}_i + \boldsymbol{T}_{i'} = \boldsymbol{0}$. Next, based on the motion equation, the time-domain integral format of the displacement of the contact system node is derived, and the normal contact force $\boldsymbol{N}_i$, $\boldsymbol{N}_{i'}$ and tangential contact force $\boldsymbol{T}_i$, $\boldsymbol{T}_{i'}$ are solved.

After the finite element discretization of the contact system of surrounding rock and fault, the motion equation of the contact system node is

$$\boldsymbol{M}\ddot{\boldsymbol{u}} + \boldsymbol{C}\dot{\boldsymbol{u}} + \boldsymbol{K}\boldsymbol{u} = \boldsymbol{F} + \boldsymbol{N} + \boldsymbol{T} \tag{12}$$

where $\boldsymbol{M}$, $\boldsymbol{C}$ and $\boldsymbol{K}$ are the mass, damping and stiffness matrices, respectively; $\ddot{\boldsymbol{u}}$, $\dot{\boldsymbol{u}}$ and $\boldsymbol{u}$ are the acceleration, velocity and displacement vectors of the node, respectively; $\boldsymbol{F}$ is the external load vector; $\boldsymbol{N}$ and $\boldsymbol{T}$ are the normal and tangential contact force vectors on the contact surface, respectively.

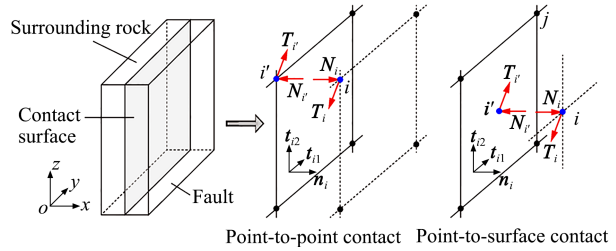

Fig. 1 Contact types and contact force on the interface

The central difference method is adopted to solve the motion equation, and the explicit integral expression of the displacement at the time step n+1 is

$$\boldsymbol{u}^{n+1} = \bar{\boldsymbol{u}}^{n+1} + \Delta\boldsymbol{u}^{n+1} \tag{13}$$

$$\bar{\boldsymbol{u}}^{n+1} = \boldsymbol{u}^n + \Delta t\dot{\boldsymbol{u}}^n + \Delta t^2\boldsymbol{M}^{-1}\left(\boldsymbol{F}^n - \boldsymbol{K}\boldsymbol{u}^n - \boldsymbol{C}\dot{\boldsymbol{u}}^n\right)/2 \tag{14}$$

$$\Delta\boldsymbol{u}^{n+1} = \Delta t^2\boldsymbol{M}^{-1}\left(\boldsymbol{N}^n + \boldsymbol{T}^n\right)/2 \tag{15}$$

where $\Delta t = t_{n+1} - t_n$ is the time step; $\boldsymbol{u}^{n+1}$ is the node displacement vector at the current time; $\bar{\boldsymbol{u}}^{n+1}$ is the node displacement vector without considering the contact force; and $\Delta\boldsymbol{u}^{n+1}$ is the additional displacement vector caused by contact force.

Based on the assumption of the average acceleration method, the velocity and acceleration at time step n+1 can be expressed as

$$\dot{\boldsymbol{u}}^{n+1} = 2(\boldsymbol{u}^{n+1} - \boldsymbol{u}^n)/\Delta t - \dot{\boldsymbol{u}}^n \tag{16}$$

$$\ddot{\boldsymbol{u}}^{n+1} = 2(\dot{\boldsymbol{u}}^{n+1} - \dot{\boldsymbol{u}}^n)/\Delta t - \ddot{\boldsymbol{u}}^n \tag{17}$$

According to Eqs. (16) and (17), the motion state of the node at time step n+1 can be explicitly solved according to the node displacement, velocity and dynamic contact force at time step n. The motion state at time step n is known. The contact force vectors, namely $\boldsymbol{N}^n$ and $\boldsymbol{T}^n$ at time step n should also be calculated according to the contact conditions.

3.2 Solution of contact force

3.2.1 Contact force of point-to-point contact

The point-to-point contact shown in Fig.1 assumes that the contact node pairs i and i' are in the bonding contact state at time step n+1, then it satisfies the constraint conditions of normal non-embedding and tangential non-relative displacement, i.e.

$$\begin{Bmatrix} \boldsymbol{n}_i^{\mathrm{T}} \\ \boldsymbol{t}_{i1}^{\mathrm{T}} \\ \boldsymbol{t}_{i2}^{\mathrm{T}} \end{Bmatrix}(\boldsymbol{u}_{i'}^{n+1} - \boldsymbol{u}_i^{n+1}) = \begin{Bmatrix} u_{i'1}^{n+1} - u_{i1}^{n+1} \\ u_{i'2}^{n+1} - u_{i2}^{n+1} \\ u_{i'3}^{n+1} - u_{i3}^{n+1} \end{Bmatrix} = \begin{Bmatrix} 0 \\ u_{i'2}^{n} - u_{i2}^{n} \\ u_{i'3}^{n} - u_{i3}^{n} \end{Bmatrix} \tag{18}$$

where $\boldsymbol{n}_i$ is the unit normal vector of node i on the contact surface, pointing from i' to i; $\boldsymbol{t}_{i1}$ and $\boldsymbol{t}_{i2}$ are two tangential unit vectors of node i; $\boldsymbol{u}_i$ and $\boldsymbol{u}_{i'}$ are the displacement vectors of nodes i and i' in the global coordinate system, respectively; the subscripts 1, 2 and 3 of $\boldsymbol{u}$ represent the components of node displacement along the normal $\boldsymbol{n}_i$ and two tangential ($\boldsymbol{t}_{i1}$, $\boldsymbol{t}_{i2}$) directions of contact surface, respectively.

Substitute Eq. (13) into Eq. (18), and according to the interaction between contact forces, it yields

$$\begin{Bmatrix} \boldsymbol{N}_i^n \\ \boldsymbol{T}_{i1}^n \\ \boldsymbol{T}_{i2}^n \end{Bmatrix} = \frac{2M_iM_{i'}}{(M_i + M_{i'})\Delta t^2}\begin{Bmatrix} (\bar{u}_{i'1}^{n+1} - \bar{u}_{i1}^{n+1})\boldsymbol{n}_i \\ [\bar{u}_{i'2}^{n+1} - \bar{u}_{i2}^{n+1} - (u_{i'2}^{n} - u_{i2}^{n})]\boldsymbol{t}_{i1} \\ [\bar{u}_{i'3}^{n+1} - \bar{u}_{i3}^{n+1} - (u_{i'3}^{n} - u_{i3}^{n})]\boldsymbol{t}_{i2} \end{Bmatrix} \tag{19}$$

where $\boldsymbol{N}_i^n$ is the normal contact force vector of the node

I; and $\boldsymbol{T}_{i1}^n$, $\boldsymbol{T}_{i2}^n$ are the tangential contact force vectors of node i, $\boldsymbol{T}_i^n=\boldsymbol{T}_{i1}^n+\boldsymbol{T}_{i2}^n$.

3.2.2 Contact force of point-to-surface contact

Figure 1 also illustrates the point-to-surface contact form, it is assumed that the contact node pairs i and point i' on the unit surface are in bonding contact state at time step n+1. The displacement of contact point i' can be calculated by shape function interpolation:

$$\boldsymbol{u}_{i'}^n=\sum_j \phi_j \boldsymbol{u}_j^n,\ \ \overline{\boldsymbol{u}}_{i'}^{n+1}=\sum_j \phi_j \overline{\boldsymbol{u}}_j^{n+1} \tag{20}$$

Similarly, the equivalent concentrated mass $M_{i'}$ of contact point i' can be calculated as follows:

$$M_{i'}=\sum_j m_j \tag{21}$$

$$m_j=\phi_j M_j \Big/ \sum_l \phi_l^2 \tag{22}$$

where j is marked as the node of i'; ϕ_j is the value of shape function of node j at contact point i'; m_j represents the mass contribution of node j at contact point i'; and M_j is the concentrated mass of node j.

According to the contact displacement constraints and interaction forces, Eq. (19) is finally derived, and the contact force at node i in the form of point-to-surface contact can then be obtained by substituting Eqs. (20) and (21) into Eq. (19).

3.2.3 Modification of contact state and contact force

The expressions of dynamic contact forces in point-to-point and point-to-surface contact forms are calculated based on the assumption of bonding contact. Therefore, in each calculation step, it is necessary to determine whether it is in the slip or detachment contact state and then modify the corresponding contact forces.

First, the ultimate contact forces at contact node i should be determined according to the shear strength model of the contact surface in the previous section. If the contact node is in the state of bonding contact until the time step n, its tensile force P_{iN}^n and shear force P_{iT}^n can be expressed as

$$P_{iN}^n=\sigma_{\mathrm{t}} A_i,\ \ P_{iT}^n=\tau_{\mathrm{p}}(t) A_i \tag{23}$$

where σ_{t} is the tensile strength of contact surface; A_i represents the area of node i.

If the contact node slips or separates before time step n, it indicates that the bonding interface has been damaged. In this case, the ultimate contact forces are provided by the residual strength and can be computed as

$$P_{iN}^n=0,\ \ P_{iT}^n=\tau_{\mathrm{r}}(t) A_i \tag{24}$$

According to the ultimate contact forces, the contact state is checked and the contact forces are corrected according to the following two scenarios:

(1) If $\boldsymbol{N}_i^n \boldsymbol{n}_i<0$, the contact surface is in a tensile state. If it further satisfies $\sqrt{\left\|\boldsymbol{N}_i^n\right\|^2+\left\|\boldsymbol{T}_{i1}^n\right\|^2+\left\|\boldsymbol{T}_{i2}^n\right\|^2}>P_{iN}^n$, it indicates the contact nodes are disconnected. Under this circumstance, the contact forces are modified according to the following formula:

$$\boldsymbol{N}_i^n=0,\ \boldsymbol{T}_{i1}^n=0,\ \boldsymbol{T}_{i2}^n=0 \tag{25}$$

(2) If $\boldsymbol{N}_i^n \boldsymbol{n}_i>0$, the contact surface is in a compressive state, the tangential contact forces need to be checked. If $\sqrt{\left\|\boldsymbol{T}_{i1}^n\right\|^2+\left\|\boldsymbol{T}_{i2}^n\right\|^2}>P_{iT}^n$, that means there is some slippage at the contact point. The tangential contact forces need to be corrected by the following formula:

$$\left.\begin{aligned}\boldsymbol{T}_{i1}^n&=\tau_{\mathrm{r}}(t) A_i \cdot \boldsymbol{T}_{i1}^n \Big/ \sqrt{\left\|\boldsymbol{T}_{i1}^n\right\|^2+\left\|\boldsymbol{T}_{i2}^n\right\|^2}\\ \boldsymbol{T}_{i2}^n&=\tau_{\mathrm{r}}(t) A_i \cdot \boldsymbol{T}_{i2}^n \Big/ \sqrt{\left\|\boldsymbol{T}_{i1}^n\right\|^2+\left\|\boldsymbol{T}_{i2}^n\right\|^2}\end{aligned}\right\} \tag{26}$$

The contact state between surrounding rock and fault contact surface at time step n+1 is gained through the above calculations. By substituting the dynamic contact forces into Eqs. (13)−(17), the motion state of each node in the contact system at time step n+1 can be obtained.

This 3D dynamic contact force algorithm is more suitable for the whole fault zone across the workshop, and is favorable to simulate the bond, slip and detachment between surrounding rock and fault during the earthquake.

4 Seismic response analysis of cavern

4.1 Project overview

Jinchuan hydropower station is one of the most important hydropower projects in the Dadu River region in Southwest China. The main workshop size is 124.5 m× 25.8 m×64.25 m (length×width×height), with large spans and high sidewalls. The geological survey found that a steeply dipped fault F31 cuts diagonally into the main workshop. Its occurrence is NW324° NE∠85°, and it is a grade II structural plane with an extension length of more than 500 m and a width of about 2.0 m. The fault is filled with mylonite, fault gouge and a small amount of fragmental rock. The strike of fault F31 is inclined to the axis of the workshop at 36° and crosses the whole workshop. As is suggested by the geological survey, fault F31 greatly influences the stability of high sidewall surrounding rock in the upstream and downstream of the workshop. The basic intensity of earthquake is rated as 7, and the fault zone is the weak link of seismic resistance of the underground cavern.

4.2 Computation model and conditions

4.2.1 3D finite element model

Figure 2 presents the finite element model of the underground powerhouse with the F31 fault, which is

excavated in 9 stages. The *x*-axis is perpendicular to the axis of the workshop and points to the west, *y*-axis points to the south along the axis of the workshop, and the *z*-axis is straight up. The model size in three directions is 180.0, 224.5 m and 160.0 m, respectively. The calculation model is mainly composed of hexahedral isoparametric elements and locally supplemented by degenerate elements, subdividing into 170 282 elements and 125 781 nodes. The maximum element size does not exceed 6 m to meet the requirements of dynamic calculation accuracy. Before calculation, the common nodes of the surrounding rock and the fault are separated to form the contact surface to establish the initial contact pair.

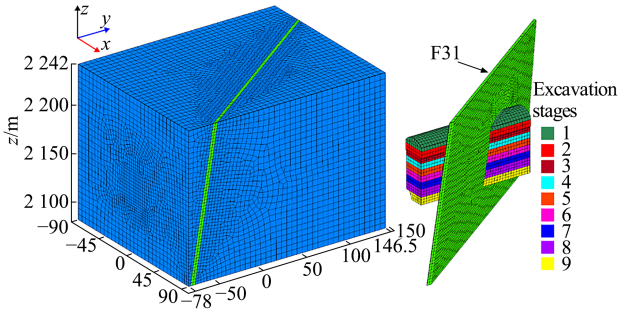

Fig. 2 Finite element model

Monitoring points P1 and P2 are respectively arranged in surrounding rock and fault at an elevation of 2 148 m in the middle of the downstream sidewall of the main workshop, as shown in Fig.3. For the convenience of analysis, the contact surface between the fault and its hanging wall surrounding rock is marked as face 1, while the contact surface between the fault and its footwall surrounding rock is marked as face 2.

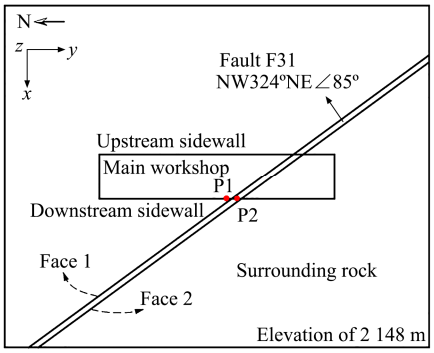

Fig. 3 Layout of monitoring points

4.2.2 Computation conditions

The computation program is based on the self-developed dynamic analysis platform[31], and embedded in the dynamic contact force algorithm, which takes complex shear strength and multiple contact states into account. According to the suggested values in the geological survey report, the initial rock mass mechanical parameters of surrounding rock and fault are listed in Table 1. The relevant parameters of the contact surface cannot be tested due to the limited conditions, and are selected according to the geological survey data and relevant empirical formulas, as shown in Table 2. Among them, JCS is chosen as the compressive strength of the fault. The value of JRC is 16.0 based on experiences because of the rough and slightly undulating contact surface between fault and surrounding rock. As for the values of R_0 and ξ, according to the initial calculation, it is known that the contact surface has at least 10 cycles of shear and the maximum amplitude exceeds 15 mm. In combination with the test curve in reference [28], $R_0 = 0.8$, $\xi = 5.0$. m, q and p are evaluated according to the experimental fitting curves in literature [27]. The tensile strength of the contact surface is assumed to be mainly provided by cohesion and is set at 0.1 MPa.

Table 1 Mechanical parameters of rockmass

Type	Deformation modulus /GPa	Poisson's ratio	Density /(g • cm^{-3})	Cohesion /MPa	Friction angle /(°)	Compressive strength /MPa
Surrounding rock	9.5	0.27	2.7	1.0	43.5	70
Fault	1.1	0.35	2.7	0.1	23.3	40

Table 2 Mechanical parameters of interface

JCS /MPa	JRC	Friction angle /(°)	Seismic deterioration coefficient					Tensile strength /MPa
			R_0	ξ	m	q	p	
40	16	30.0	0.8	5	0.883	0.02	0.032	0.1

The dynamic elastoplastic yield criterion based on Mohr−Coulomb criterion is adopted for rock element[31], which is formulated as

$$\left.\begin{aligned} f^{\mathrm{s}} &= \sigma_1 - \sigma_3 N_\varphi + 2(1-D)c(\dot{\varepsilon})\sqrt{N_\varphi} = 0 \\ f^{\mathrm{t}} &= \sigma_3 - \sigma^{\mathrm{t}} = 0 \end{aligned}\right\} \tag{27}$$

where f^{s} and f^{t} are the shear and tensile yield functions, respectively; σ_1 and σ_3 are the maximum and minimum principal stresses after damage; σ^{t} is the tensile strength; $N_\varphi = (1-\sin\varphi)/(1+\sin\varphi)$; $c(\dot{\varepsilon})$ is the cohesion related to strain rate; and D is the damage coefficient, and its value is

$$\left.\begin{aligned} D_k &= 1 - \exp(-R\sqrt{\varepsilon_k^{\mathrm{p}}\varepsilon_k^{\mathrm{p}}}) \quad (k = 1, 2, 3) \\ D &= \sqrt{D_1^2 + D_2^2 + D_3^2} \end{aligned}\right\} \tag{28}$$

where D_k is the damage coefficient of the k-th principal strain direction, k = 1, 2, 3; $\varepsilon_k^{\mathrm{p}}$ is the plastic deviatoric strain in the k-th principal strain direction; and R is the damage constant.

The numerical simulation includes two steps: static excavation and dynamic calculation. In the first step, according to the in-situ stress test, the coefficients of lateral pressure in x, y and z directions are 1.1, 0.9 and

1.0, respectively. The maximum embedment depth of the main workshop is 250 m. The overburden weight is applied at the top of the model, the bottom is fixed, and the lateral normal constraint is applied. The main workshop is excavated in 9 stages from top to bottom. The static calculation is also based on the dynamic analysis platform, which is solved by setting non-viscous damping. The dynamic contact force algorithm is used to solve the contact state between the surrounding rock and fault.

The second step is dynamic calculation. The stress field and contact state after static excavation are the initial conditions of dynamic analysis. The model adopts a free field artificial boundary at the side and a viscoelastic artificial boundary at the bottom. The viscoelastic artificial boundary is also adopted at the top, and the propagation of outer wave and reflected wave in the semi-infinite domain is considered[32]. Local damping is used and the critical damping ratio is 5%, with a damping coefficient of 0.157 1[33].

The Kobe wave of Hanshin, Japan, is selected as the seismic wave in the north−south direction, of which 15 s with strong seismic fluctuation is truncated as the incident wave. According to the seismic fortification intensity of the Jinchuan hydropower project, the peak acceleration of the incident wave is adjusted to −1.5 m/s^2, pointing to the negative direction of the coordinate system. The acceleration time-history curve and Fourier spectrum curve obtained after filtering and baseline correction are shown in Fig.4. The seismic wave is the shear wave incident vertically from the bottom of the model, and the vibration direction is x−direction perpendicular to the axis of the workshop.

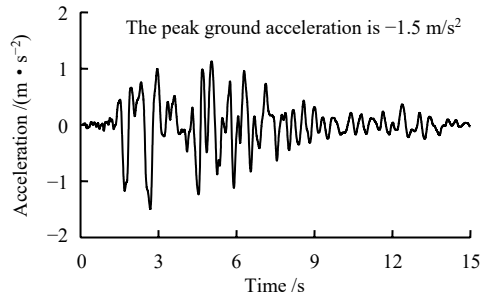

(a) Acceleration time history

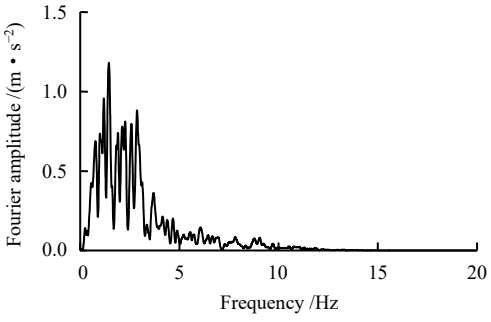

(b) Fourier spectrum

Fig. 4 Time-history and Fourier spectrum of input seismic acceleration

In this study, three working scenarios are set up for comparative analysis: (1) the contact surface is not considered; (2) the contact surface is considered, but the deterioration effect is not considered; (3) both the contact surface and the deterioration effect are considered.

4.3 Results analysis

4.3.1 Displacement characteristics of the surrounding rock

Under cyclic seismic loading, complex dynamic contact behavior occurs on the contact surface between the surrounding rock and fault, resulting in relative displacement. As reflected from the x−direction time history curves of relative displacement of P1 and P2 under three working scenarios (Fig.5), the relative displacement is very small when the contact surface is not taken into account, but the surrounding rock and fault are obviously misaligned when the contact surface is considered (scenarios 2 and 3), and the relative displacement increases rapidly between 1.0 s and 8.3 s. The maximum relative displacement of scenario 3 is 20.5 cm, which is 4.4 cm larger than that of scenario 2. The results highlight that the dynamic contact force algorithm can effectively simulate the discontinuity of surrounding rock and fault, and the relative dislocation is intensified by considering the seismic deterioration effect.

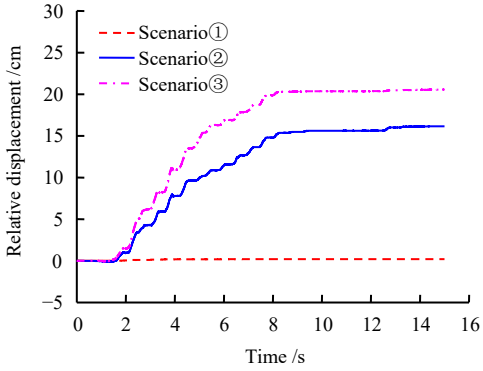

Fig. 5 Time-history curves of relative displacement in x direction of monitoring points P1 and P2

Figure 6 depicts the time-history curve of the seismic deterioration coefficient of contact surface near the monitoring points. Subjected to cyclic shear load and shear deformation rate, $D(t)$ tends to decrease exponentially with time. Between 1.0 s and 8.0 s, $D(t)$ decays rapidly and fluctuates violently affected by the shear deformation rate of the contact surface, with a minimum value of about 0.75. After 8.0 s, due to the attenuation of input seismic acceleration, $D(t)$ fluctuates from 0.77 to 0.81, mainly affected by the shear deformation rate. The time-history curve of the seismic deterioration coefficient $D(t)$ directly reflects the deterioration degree of the interface between

surrounding rock and fault at different time.

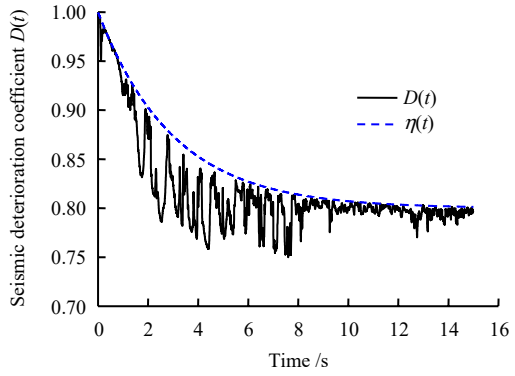

Fig. 6 Time-history curves of seismic deterioration coefficient

After the earthquake, the x−direction displacement along the axis in the middle of the upstream and downstream sidewalls of the main workshop is shown in Fig.7. The deformation stability of the workshop is primarily controlled by the steeply dipped fault. Seismic activity evidently magnifies the deformation of rock mass in the fault zone. After considering the contact surface, obvious discontinuous deformation occurs near the surrounding rock and fault interface. Because the downstream sidewall is far away from the end wall and the height of the sidewall is larger, the relative displacement of the downstream sidewall is more significant than that of the upstream sidewall.

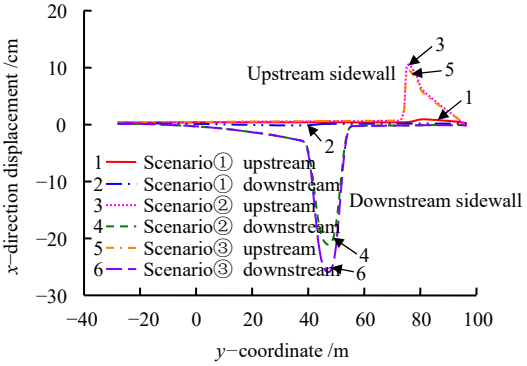

Fig. 7 Displacement distribution of sidewalls along axis *x* direction after earthquake

4.3.2 Damage characteristics of the surrounding rock

During the earthquake, the plastic failure volume and tensile failure volume of the surrounding rock gradually accumulate. The time-history curves of rock failure volume under three scenarios are plotted in Fig.8. During the period of 1−8 s with severe fluctuation, the seismic damage volume of rock increases obviously, and the failure volumes of scenarios 2 and 3 are significantly larger than that of scenario 1, with an increment of about 10.6×10^4 m^3. The main reason is that the mutual restraint between the surrounding rock and fault is weakened after the slip or detachment failure of contact surface caused by seismicity, which leads to the increase of damage and failure. The failure volume of scenario 3 is slightly larger than that of scenario 2. The volume difference between them fluctuates and the final volume difference is about 360 m^3. It is confirmed that seismic deterioration aggravates the failure of the rock mass. It can be seen that considering the contact surface and seismic deterioration effects, the damage range of cavern increases and accumulates during seismicity process.

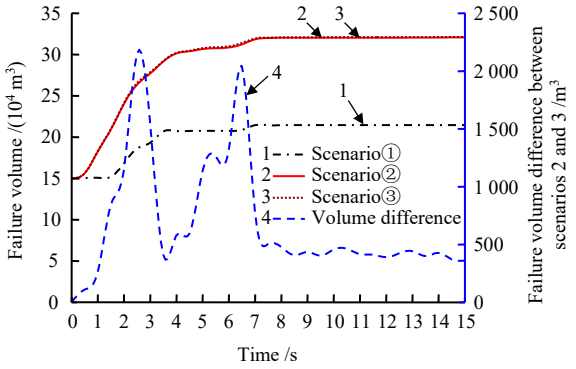

Fig. 8 Failure volume time-history curves of rockmass

Figure 9 shows the distribution of surrounding rock damage coefficient on the upstream and downstream surfaces of the main workshop after the earthquake in scenario 3. The failure zone of surrounding rock is mainly concentrated around the cavern, and the rock mass near the fault zone is seriously damaged. The failure zone develops deeply along the fault, and the damage coefficients of the fault footwall at the upstream sidewall and the hanging wall at the downstream sidewall are larger, with the maximum damage coefficient approaching 1.0. The result is similar to the deformation shown in Fig.7. Cut by the fault with a small incline angle and steeply dipped angle, the surrounding rock on one side of the high sidewall is thinner. The damage and deformation of this region are more severe than that of the other side and are significantly affected by seismic disturbance.

4.3.3 Detachment and slip of contact surface

In order to further study the failure rule of the contact surface between the surrounding rock and fault under seismic event, Fig.10 shows the detachment and slip distribution of the contact surface face 1 between the fault and surrounding rock on the hanging wall and face 2 between the surrounding rock on the footwall before and after the earthquake. Before the earthquake, the unloading caused by excavation makes the contact surface separate and slip at a certain depth of the free face. The detachment zone mainly occurs in the middle of the downstream sidewall of face 1 and the middle of the upstream sidewall of face 2, and the depth is between 3−8 m along the strike

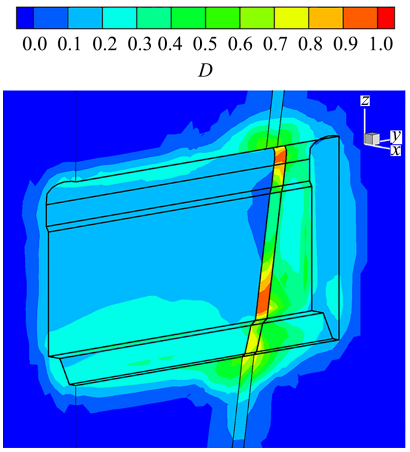

(a) Upstream face

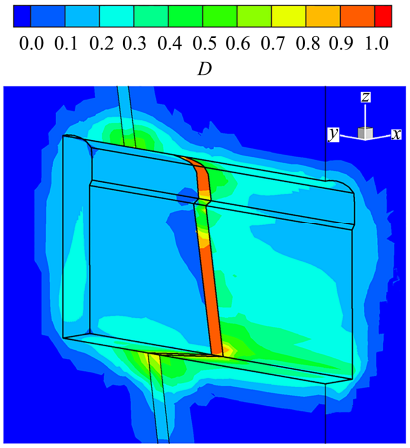

(b) Downstream face

Fig. 9 Damage coefficient distributions of upstream and downstream faces

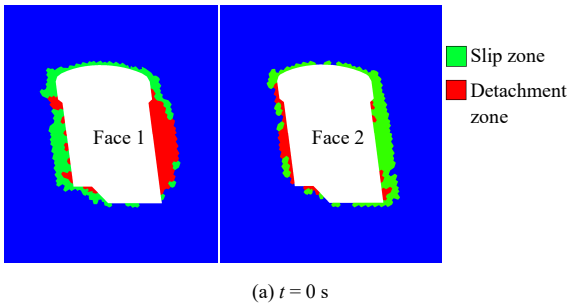

(a) t = 0 s

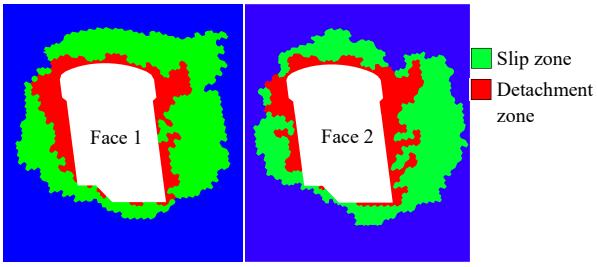

(b) t =15 s

Fig. 10 Detachment and sliding zone distributions of interfaces before and after earthquake

of the fault. During the earthquake, the slip and detachment zone of contact surface changes dynamically, along with increasing damage range. After the earthquake, the slip and detachment zones of the contact surface of the fault hanging wall and footwall are similar. Along the fault strike, the maximum slip depth of the upstream sidewall is 24.4 m, and the maximum detachment depth is 12.2 m. The maximum slip zone depth along the fault strike of the downstream sidewall is 36.6 m and the maximum detachment zone depth is 18.2 m. The damage depth of the contact surface of the downstream sidewall is more profound than that of the upstream sidewall. Under the influence of stress concentration and earthquake, the detachment zone depth of the contact surface between the arch and anchor beam is enlarged. It can be concluded that the seismicity intensifies the discontinuous deformation and failure of surrounding rock and fault accompanied by continuous extension to the interior.

4.4 Failure mechanism of cavern under steeply dipped fault

According to the numerical simulation results, it is found that the failure of surrounding rock prevailingly occurs near the steeply dipped fault, and the stability of the high sidewall of the main workshop is affected observably. As shown in Fig.11, two typical sections of fault F31 passing through the upstream and downstream sidewalls of the workshop are selected to analyze the deformation and failure mechanism of surrounding rock:

(1) Steeply dipped fault F31 with small incline angle cuts a relatively thin surrounding rock region on the high sidewall, including fault footwall at the upstream sidewall and hanging wall at the downstream sidewall. These areas are adjacent to the free face and fault zone, and the 64.25 m ‘high sidewall effect’ provides the deformation space, and the force and bending moment for failure. The seismic load amplifies the broken surrounding rock and fault zone with weak mechanical properties, resulting in large deformation and damage, which weakens its bearing capacity. When the bearing capacity is lower than the force and bending moment, failure occurs. In the upstream sidewall, the fault is an unfavorable occurrence in the upstream of steep dip. The rock mass in the weak zone and the rock mass in the fault zone are prone to bending and toppling deformation into the cavern. There is a possibility of slippage along the fault plane in the downstream sidewall into the steep dip cavern.

(2) Under the seismic action, the surrounding rock and fault interface failure occur at a certain depth, such as slip and detachment. The mian reason is the seismic amplification effect in the fault zone makes it inconsistent with the deformation of surrounding rock on the hanging wall and footwall. When the tensile stress generated by the relative deformation exceeds the tensile strength of the contact surface, it leads to detachment; similarly, when the shear stress exceeds the shear strength, slip occurs.

Meanwhile, the cyclic shear action and the relative shear deformation rate of seismic load on the contact surface also cause the deterioration of shear strength, and aggravate the discontinuous deformation failure of the contact surface. Most of the contact surfaces near the weak zone have separating failure, which further exacerbates the damage and deformation failure of the surrounding rock.

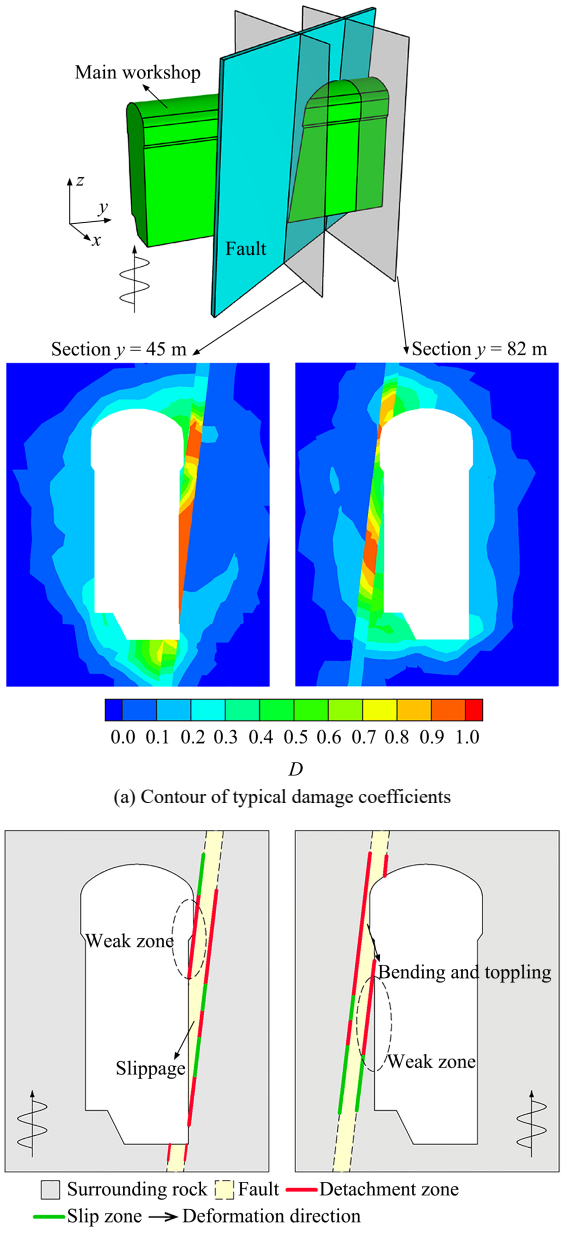

(a) Contour of typical damage coefficients

(b) Schematic of deformation and damage mode of typical surrounding rock sections

Fig. 11 Seismic damage characteristics of the main workshop intersected by a steeply dipped fault

5 Conclusions

In this study, a complex nonlinear shear strength model of surrounding rock and fault under seismic action is established, and a 3D dynamic contact force algorithm considering complex shear strength and multiple contact states is proposed. The seismic failure characteristics of the Jinchuan underground powerhouse under steeply dipped fault are studied. The following conclusions are drawn:

(1) The existence of fault enlarges the deformation and failure range of the cavern, and the seismic response becomes more severe after taking the seismic deterioration effect of the contact surface into account. Under the influence of earthquakes, the dislocation of surrounding rock and fault is intensified, and slip and detachment failure at a certain depth occur. It reveals that the proposed algorithm can effectively reflect the seismic deterioration effect of the contact surface and simulate the nonlinear large slip phenomenon of surrounding rock and fault under seismic action.

(2) The steeply dipped fault cuts the main workshop obliquely, resulting in a weak zone with thin surrounding rock thickness. The seismic response has a pronounced amplification effect in these weak zones and fault zones, causing a large deformation and damage. The weak zone is prone to bending and toppling deformation in the upstream sidewall and sliding along the fault plane in the downstream sidewall.

(3) The distribution of the slip and detachment failure zone on the interface evolves dynamically with the seismicity process and extends to the depth of the surrounding rock. The contact surface damage depth of the downstream sidewall of the workshop through the steeply dipped fault is more significant than that of the upstream sidewall, and the detachment zone of the arch seat and anchor beam is larger.

(4) The numerical simulation results highlight the seismic response characteristics and failure mechanism of the underground cavern intersected by a steeply dipped fault, which can provide references for the seismic design of similar projects.

References

[1] CUI Zhen, SHENG Qian, LENG Xian-lun, et al. A review of study on seismic catastrophe of large-scale underground cavern group[J]. Journal of Disaster Prevention and Mitigation Engineering, 2013, 33(5): 606−616.

[2] LI Tian-bin. Failure characteristics and influence factor analysis of mountain tunnels at epicenter zones of great Wenchuan earthquake[J]. Journal of Engineering Geology, 2008, 16(6): 742−750.

[3] QIAN Qi-hu, HE Chuan, YAN Qi-xiang. Dynamic response characteristics and lessons learnt from damage of tunnels in Wunchuan earthquake[C]//Investigation, Analysis and Research of Seismic Damages in Wenchuan Earthquake. Beijing: Science Press, 2009: 773−778.

[4] DENG S X, LI J, JIANG H M, et al. Experimental and theoretical study of the fault slip events of rock masses around underground tunnels induced by external disturbances[J]. Engineering Geology, 2018, 233: 191−199.

[5] TRIFONOV O V, CHERNIY V P. A semi-analytical approach to a nonlinear stress-strain analysis of buried steel pipelines crossing active faults[J]. Soil dynamics and Earthquake Engineering, 2010, 30(11): 1298−1308.

[6] MAO Hao-yu, XU Nu-wen, LI Biao, et al. Stability analysis of an underground powerhouse on the left bank of the Baihetan hydropower station based on discrete element simulation and microseismic monitoring[J]. Rock and Soil Mechanics, 2020, 41(7): 2470−2484.

[7] HE Chuan, LI Lin, ZHANG Jing, et al. Seismic damage mechanism of tunnels through fault zones[J]. Chinese Journal of Geotechnical Engineering, 2014, 36(3): 427− 434.

[8] LI Lin, HE Chuan, GENG Ping, et al. Analysis of seismic dynamic response of tunnel through fault zone in high earthquake intensity area[J]. Journal of Chongqing University, 2012, 35(6): 92−98.

[9] ZHAO Mi, OU YANG Wen-long, HUANG Jing-qi, et al. Analysis of axis dynamic response of rock tunnels through fault fracture zone under P waves of earthquake[J]. Rock and Soil Mechanics, 2019, 40(9): 3645−3655.

[10] YANG Z, LAN H, ZHANG Y, et al. Nonlinear dynamic failure process of tunnel-fault system in response to strong seismic event[J]. Journal of Asian Earth Sciences, 2013, 64: 125−135.

[11] ARDESHIRILAJIMI S, YAZDANI M, ASSADI LANGROUDI A. Control of fault lay-out on seismic design of large underground caverns[J]. Tunnelling and Underground Space Technology, 2015, 50: 305−316.

[12] CUI Zhen, SHENG Qian, LENG Xian-lun, et al. Control effect of large geological discontinuity on seismic response and stability of underground rock caverns[J]. Rock and Soil Mechanics, 2018, 39(5): 1811−1824.

[13] WANG X W, XIONG Q R, ZHOU H, et al. Three-dimensional (3D) dynamic finite element modeling of the effects of a geological fault on the seismic response of underground caverns[J]. Tunnelling and Underground Space Technology, 2020, 96: 103210.

[14] ZHANG Z Q, CHEN F F, LI N, et al. Influence of fault on the surrounding rock stability of a tunnel: location and thickness[J]. Tunnelling and Underground Space Technology, 2017, 61: 1−11.

[15] ZHANG Bo-hu, DENG Jian-hui, ZHOU Zhi-hui, et al. Analysis of monitoring microseism in areas controlled by faults near powerhouse in Dagangshan hydropower station[J]. Rock and Soil Mechanics, 2012, 33(Suppl.2): 213−218.

[16] LI Ang, DAI Feng, XU Nu-wen, et al. Failure mechanism and mode of surrounding rock of underground powerhouse at the right bank of Wudongde hydropower station subjected to excavation[J]. Chinese Journal of Rock Mechanics and Engineering, 2017, 36(4): 781−793.

[17] LI Xiao-feng, LI Hai-bo, XIA Xiang, et al. Numerical simulation of mechanical characteristics of jointed rock in direct shear test[J]. Rock and Soil Mechanics, 2016, 37(2): 583−591.

[18] FOX D J, KAÑA D D, HSIUNG S M. Influence of interface roughness on dynamic shear behavior in jointed rock[J]. International Journal of Rock Mechanics and Mining Sciences, 1998, 35(7): 923−940.

[19] BARTON N, CHOUBEY V. The shear strength of rock joints in theory and practice[J]. Rock Mechanics, 1977, 10(1-2): 1−54.

[20] PATTON F D. Multiple modes of shear failure in rock[C]// The First Congress of International Society of Rock Mechanics. Lisbon: [s. n.], 1966: 509−513.

[21] LADANYI B, ARCHAMBAULT G. Simulation of shear behavior of a jointed rock mass[C]//The 11th US Rock Mechanics Symposium (USRMS). Berkeley: [s. n.], 1969: 105−125.

[22] GRASSELLI G, EGGER P. Constitutive law for the shear strength of rock joints based on three-dimensional surface parameters[J]. International Journal of Rock Mechanics and Mining Sciences, 2003, 40(1): 25−40.

[23] GHAZVINIAN A H, AZINFAR M J, GERANMAYEH VANEGHI R. Importance of tensile strength on the shear behavior of discontinuities[J]. Rock Mechanics and Rock Engineering, 2012, 45(3): 349−359.

[24] XIE He-ping, CHEN Zhong-hui, YI Cheng, et al. Research on deformation and failure of interface based on interaction between structural body and geo-body[J]. Chinese Journal of Rock Mechanics and Engineering, 2008, 27(9): 1767−1780.

[25] YANG Z Y, LO S C, DI C C. Reassessing the joint roughness coefficient (JRC) estimation using Z_2[J]. Rock Mechanics and Rock Engineering, 2001, 34(3): 243−251.

[26] LEE H S, PARK Y J, CHO T F, et al. Influence of asperity degradation on the mechanical behavior of rough rock joints under cyclic shear loading[J]. International Journal of Rock Mechanics and Mining Sciences, 2001, 38(7): 967−980.

[27] LI Hai-bo, FENG Hai-peng, LIU Bo. Study on strength behaviors of rock joints under different shearing deformation velocities[J]. Chinese Journal of Rock Mechanics and Engineering, 2006, 25(12): 2435−2440.

[28] NI Wei-da, TANG Hui-ming, LIU Xiao, et al. Dynamic stability analysis of rock slope considering vibration deterioration of structural planes under seismic loading[J]. Chinese Journal of Rock Mechanics and Engineering, 2013, 32(3): 492−500.

[29] ZHOU H, XIAO M, YANG Y, et al. Seismic response analysis method for lining structure in underground cavern of hydropower station[J]. KSCE Journal of Civil Engineering, 2019, 23(3): 1236−1247.

[30] LIU Guo-qing, XIAO Ming, YANG Yang, et al. Numerical simulation and analysis method of seismic response for hydraulic tunnel across fault[J]. Journal of Hunan University (Natural Sciences), 2018, 45(11): 140−148.

[31] ZHANG Zhi-guo, XIAO Ming, CHEN Jun-tao. Simulation of earthquake disaster process of large-scale underground caverns using three-dimensional dynamic finite element method[J]. Chinese Journal of Rock Mechanics and Engineering, 2011, 30(3): 509−523.

[32] ZHANG Z G, CHEN J T, XIAO M. Artificial boundary setting for dynamic time-history analysis of deep buried underground caverns in earthquake disaster[J]. Disaster Advances, 2012, 5(4): 1136−1142.

[33] ZHENG Ying-ren, YE Hai-lin, HUANG Run-qiu. Analysis and discussion of failure mechanism and fracture surface of slope under earthquake[J]. Chinese Journal of Rock Mechanics and Engineering, 2009, 28(8): 1714−1723.